ACS APPLIED ENGINEERING MATERIALS

pubs.acs.org/acsaenm Article

Exploring the Electronic Structure and Interfacial Phenomena of Pseudomorphic Rutile(110) Heterostructures: An Ab Initio Study

S. Muthukrishnan, R. Vidya,* and Anja Olafsen Sjåstad

Cite This: ACS Appl. Eng. Mater. 2025, 3, 2141−2152 Read Online

ABSTRACT: The photocatalytic application of pure TiO_2 is limited because of its wide band gap, which restricts its activity only in the UV (ultraviolet) region of the solar spectrum. The high recombination of electron and hole charge carriers is another drawback to photocatalytic activity. In this work, we explore the electronic interfacial characteristics of pseudomorphic rutile(110) heterostructures, such as SnO_2/TiO_2, NbO_2/TiO_2, and MnO_2/TiO_2, using density functional theory (DFT)-based computations. The nature of the electronic structure and the band alignment are studied, which helps to identify the heterostructure. The internal electric field created at the interface of the heterostructure is crucial for defining the flow of electron and hole charge carriers, which is understood by the charge density difference plots. The enhancement of optical absorption of the heterostructure toward the visible region of the solar spectrum is further confirmed. From our analysis, we conclude that the nature of the electronic structure and band alignment of the rutile heterostructure are explored. Here, SnO_2/TiO_2 shows a type II heterostructure, MnO_2/TiO_2 shows a type I heterostructure, and NbO_2/TiO_2 shows a metal−semiconductor interface. From the heterostructure model, we proved that the band gap can be reduced toward the visible light absorption, and also, the electron and hole recombination can be avoided by generating the internal electric field along the interface of the heterostructure. From our analysis, we conclude that the pseudomorphic rutile(110) heterostructure will act as a potential photocatalyst for environmental pollution reduction.

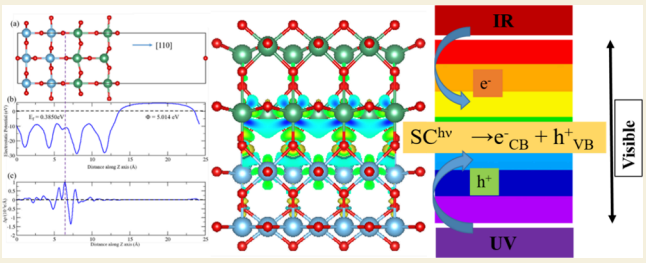

KEYWORDS: *pseudomorphic heterostructure, density functional theory, internal electric field, band alignment, optical absorption*

1. INTRODUCTION

TiO_2 is considered the most promising semiconductor photocatalyst for its advantages, such as chemical stability, nontoxicity, low cost, and biocompatibility.[1] The photolysis of water by TiO_2 makes it useful for various environmental applications such as hydrogen production, water treatment, antifogging applications, organic synthesis, and environmental pollution reduction.[2] However, some of the disadvantages of TiO_2, such as its large band gap and higher recombination of photogenerated charge carriers, restrict its photocatalytic efficiency. Many methodologies are followed to reduce its band gap and also to improve its photocatalytic activity by metal doping, nonmetal doping, and the formation of semiconductor heterojunctions.[3] Our previous study showed that TiO_2 can be made into visible-light-active photocatalysts by transition metal doping and codoping.[4] Among various surfaces, TiO_2 rutile(110) is the most stable and has superior photocatalytic properties.[5] TiO_2 rutile(110) can be used for the photodegradation of harmful pollutants.[6]

For large-scale industrial applications, heterostructures should be cost-effective, and they should be based on the Earth's abundant materials. Hence, in this work, the heterostructure is based on TiO_2- and SnO_2-based materials. These are generally considered low-cost materials for the heterostructure construction. Another very important factor in the large-scale industrial production of photocatalytic materials is their stability. Here, we used TiO_2-based materials as the heterostructure model construction, and TiO_2 is known for its most prominent photostability and thermal and chemical stability. Some literature shows evidence that heterostructure construction can also enhance the stability of the materials. Scalability is considered another important factor that influences the industrial-scale production of photocatalytic materials. Achieving the uniform morphology and maintaining the interfacial contact are considered some of the challenges in the scalability of the photocatalytic materials.[44,45]

Compared to the bare TiO_2 surfaces, the heterostructure of other transition metal oxides deposited on top of TiO_2 attracts considerable interest due to their enhanced photocatalytic properties and enhanced separation of electron and hole charge carriers.[7] Lin et al. fabricated the MoS_2/TiO_2

Received: May 1, 2025
Revised: June 23, 2025
Accepted: June 24, 2025
Published: June 30, 2025

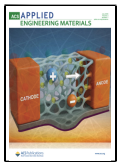

https://doi.org/10.1021/acsaenm.5c00313
ACS Appl. Eng. Mater. 2025, 3, 2141−2152

heterostructure by the hydrothermal method and found that this heterostructure exhibits superior photocatalytic properties for the degradation of Rhodamine B, compared to pure TiO_2.[8] Similarly, the Bi_2O_3/TiO_2 heterostructure exhibits superior photocatalytic degradation of ofloxacin than pure TiO_2.[9] The one-dimensional heterostructure of $CeVO_4/TiO_2$ shows higher photocatalytic degradation compared to bare $CeVO_4$ and TiO_2.[10] The ZnO/TiO_2 heterostructure,[11] prepared by the hydrothermal method, shows good photocatalytic activity with a higher hydrogen production rate compared to bare TiO_2 and ZnO. The heterostructure model has enhanced light absorption and also has superior separation of electron and hole charge carriers. Previously, several studies regarding the heterostructure have been reported and are discussed in the following.

The SnO_2/TiO_2 heterostructure shows improved photocatalytic activity compared to pure SnO_2 and TiO_2. Moreover, the band gap of the heterostructure can be tuned toward visible light absorption, and the recombination of electron and hole charge carriers is suppressed.[12] The Cu_2O/TiO_2 heterostructure prepared by the solvothermal method has good morphological properties with type II band alignment and shows four times higher photocatalytic reduction of CO_2 than that of pure Cu_2O.[13] The Cu_2O/TiO_2 heterostructure prepared by the electrodeposition method shows both ultraviolet and visible light absorption and a better decomposition of methylene blue than pure TiO_2.[14] The addition of NiO to TiO_2 generates an absorption band and results in increased visible light activity. Moreover, it enhances the separation of electron and hole charge carriers by the formation of a p−n junction. The photocatalytic activity can be tuned by the content of NiO.[15] The WO_3/TiO_2 heterostructure prepared by the hydrothermal method shows a band gap value of 0.5 eV lower than that of pure TiO_2.[16] Wei et al. studied the pseudomorphic RuO_2/TiO_2 heterostructure with (110) orientation by a density functional theory (DFT) study. They found that the accumulation of electron charges at the interface of the heterostructure creates an internal electric field, which further helps us to enhance the separation of electron and hole charge carriers.[17]

Yong-dong et al. studied the SnO_2/TiO_2 heterostructure in both (110) and (101) orientations with a graded and abrupt model by DFT. They reported that the graded heterostructure is more stable than the abrupt heterostructure. They also conclude that there was a generation of electric dipole moment at the interface of the heterostructure, which will enhance the separation and restrain the recombination of electron and hole charge carriers. In the heterostructure model, there was an accumulation of electrons in the conduction band (CB) of TiO_2 and holes in the valence band (VB) of SnO_2.[18] Experimental studies on the SnO_2/TiO_2 heterostructure show that it has good transport of charge carriers and also inhibits charge carrier recombination.[19] Zhang et al. synthesized the MnO_2/TiO_2 heterostructure experimentally, and they found that the heterostructure model shows enhanced photocatalytic activity for the degradation of volatile organic compounds, and also, the heterostructure has the suppression of recombination of electron and hole pairs, which eventually degrades the photocatalytic activity.[20,21] However, in the previous studies, there was no clear information regarding the structural, optical, and electrical properties of the pseudomorphic heterostructure. The exact mechanism of the charge transport process along the interface of the heterostructure has not been discussed so far.

In this work, the pseudomorphic rutile(110) heterostructure of SnO_2/TiO_2, NbO_2/TiO_2, and MnO_2/TiO_2 was considered for the DFT studies. The (110) surface of the rutile crystal structure ($P4_2/mnm$) of transition metal oxides was taken for the heterostructure model. The surface geometry and interfacial formation energy of the heterostructure are studied. The electronic structure analysis was carried out by hybrid density functional analysis calculations. The optical absorption spectra for the three different heterostructures are calculated. The electrostatic potential along the *Z*-direction of the heterostructure is derived, and the creation of an internal electric field on the heterostructure is analyzed by charge density difference plots along the interface. The chemical bonding characteristics are analyzed by charge density and electron localization function (ELF) plots. The band alignment of these heterostructures is studied, and the type of heterostructure is identified. A possible way to enhance the photocatalytic activity by tuning the heterostructure model is proposed.

2. COMPUTATIONAL DETAILS

The computational calculations are done by the DFT analysis. The plane-wave-based pseudopotential approximation is used, as implemented in the Vienna Ab initio Simulation Package (VASP).[22,23] For the exchange−correlation functional, the generalized gradient approximation with the Perdew, Burke, and Ernzerhof (GGA-PBE) formalism is followed.[24,25] For the expansion of the electron wave function, a 500 eV kinetic energy cutoff for the plane wave is used. In this work, a 3 × 1 supercell of the rutile(110) heterostructure slab model with a vacuum of 12 Å is taken to avoid the periodic boundary condition in the *Z*-direction. For the simulation, four layers of heterostructure are taken, and the bottom layer of the cell is fixed during the relaxation. A 4 × 4 × 1 Monkhorst−Pack *K*-Point sampling is taken for the Brillouin zone integration.[26] The convergence is achieved by setting threshold values as 10^{-6} eV and 0.01 eV/Å for energy and force, respectively. For force minimization, the conjugate gradient algorithm is adopted. For the accurate prediction of the band gap of the heterostructure, the hybrid functional calculations (HSE06) are used.[27] Spin-polarized calculations are carried out to consider the magnetization. For the visualization of the slab model, the VESTA package is used,[28] and for the postprocessing of the results of VASP calculations, the VASPKIT tool is used.[29] For plotting the charge density plots for the heterostructure, the XCRYSDEN tool is used.[30] The valence electrons are taken as d3s1, s2p2, 4p5s4d, d6s1, and s2p4 for Ti, Sn, Nb, Mn, and O, respectively. The amount of charge transferred along the interface of the heterostructure is calculated by the Bader charge analysis.[47] The electrostatic potential is calculated by enabling the local potential functions, as implemented in the VASP packages.[48] The chemical bonding analysis is carried out with the aid of the ELF, which is further used to find the probability of the electron pair.[49]

$$E_{\text{Form-eng}} = E_{\text{Htr}}^{\text{total}} - E_{\text{XO2}}^{\text{total}} - E_{\text{TiO2}}^{\text{total}} \quad (1)$$

The stability of the pseudomorphic rutile(110) heterostructure can be studied by calculating the interfacial formation energy of the three heterostructures. Eqn 1 can be used to calculate

https://doi.org/10.1021/acsaenm.5c00313
ACS Appl. Eng. Mater. 2025, 3, 2141−2152

the interfacial formation energy ($E_{\text{Form-eng}}$) of the heterostructure,[17] where $E_{\text{Htr}}^{\text{total}}$ is the total energy of the heterostructure, such as SnO_2/TiO_2, NbO_2/TiO_2, and MnO_2/TiO_2. $E_{\text{XO2}}^{\text{total}}$ is known as the total energy of SnO_2, NbO_2, and MnO_2 part of the heterostructure. $E_{\text{TiO2}}^{\text{total}}$ is known as the total energy of the TiO_2 portion of the surface.

3. RESULTS AND DISCUSSION

3.1. Geometrical Surface Structure

The relaxed structures of the geometrical model of the rutile(110) heterostructure of SnO_2/TiO_2, NbO_2/TiO_2, and MnO_2/TiO_2 are shown in Figure 1. The rutile(110) surface is

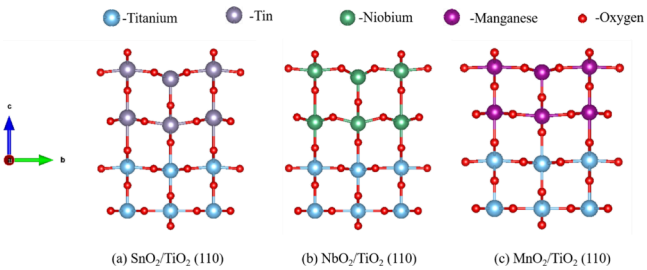

Figure 1. Relaxed structure of the 3 × 1 supercell of the SnO_2/TiO_2 (a), NbO_2/TiO_2 (b), and MnO_2/TiO_2 (c) rutile(110) heterostructure.

terminated by the 2_c (two-coordinated) bridge oxygen atom, followed by an in-plane 5_c (five-coordinated) metal atom and 3_c (three-coordinated) oxygen atoms. After the relaxation, the top layer of the heterostructure is shifted along the *Z*-direction. The 5_c metal atom (Sn, Nb, Mn) on the surface is shifted slightly downward, whereas the 6_c (six-coordinated) metal atom and 3_c oxygen atoms are shifted upward; these results agree well with our previous study.[50,31] The calculated bond lengths for bulk rutile TiO_2 are 2.009 and 1.964 Å in planar and axial directions, respectively, which also agree well with the previous study.[32,33] Similarly, the bond lengths for SnO_2, NbO_2, and MnO_2 surfaces are 2.091, 2.049, and 1.861 Å in the planar direction, respectively. The calculated bond lengths and bond angles for the bulk and surface regions of the heterostructure are shown in Table 1. Due to the surface relaxation, the angle between the O_{3c} and 6_c metal atoms (Sn, Nb, and Mn) is slightly changed, and the bond angles are 167.91°, 169.67°, and 175.55° for SnO_2, NbO_2, and MnO_2 surfaces, respectively. The calculated lattice parameters of bulk TiO_2, SnO_2, NbO_2, and MnO_2 are shown in Table S1 in the Supporting Information.

The octahedral distortions of the TiO_2, SnO_2, NbO_2, and MnO_2(110) surfaces and their heterostructure are studied and are shown in Figure 2. The bond length in both planar and axial bonds was calculated, and the corresponding bond lengths and bond angles are also shown in the figure. Here, the atomic radii (pm) for Ti, Sn, Nb, Mn, and O are 140, 145, 145, 140, and 60, respectively. Here, the angles between the axial bond and planar bonds are 86.39°, 84.20°, 80.13°, and 88.58° for TiO_2, SnO_2, NbO_2, and MnO_2 rutile(110) surfaces, respectively. Compared to all of the surfaces, the axial bonds of Nb−O have the longest bond length (Figure 2d), and Mn−O has the shortest bond length (Figure 2d). For the case of the heterostructure model, NbO_2/TiO_2 has the highest bond angle deviation of 152.10° (Figure 2f), and MnO_2/TiO_2 has a minimum bond angle deviation of 172.52° (Figure 2g). Similar

Table 1. Calculated Bond Length and Angle of the Rutile(110) Heterostructure

	SnO_2/TiO_2				NbO_2/TiO_2				MnO_2/TiO_2			
	Ti−O bond length Å (angle θ)		Sn−O bond length Å (angle θ)		Ti−O bond length Å (angle θ)		Nb−O bond length Å (angle θ)		Ti−O bond length Å (angle θ)		Mn−O bond length Å (angle θ)	
	planar	axial	planar	axial	planar	axial	planar	axial	planar	axial	planar	axial
bulk	2.009	1.964	2.091	2.089	2.009	1.964	2.049	2.091	2.009	1.964	1.861	1.877
layer 1	1.910 (180.00°)	1.947 (81.16°)	2.047 (180.00°)	1.974 (81.00°)	1.933 (180.00°)	1.947 (81.16°)	2.397 (180.00°)	2.037 (83.02°)	1.894 (180.00°)	1.947 (81.16°)	1.767 (180.00°)	1.939
			2.438				1.928				2.064	
layer 2	1.978 (171.49°)	1.926 (83.28°)	2.032 (167.91°)	1.954 (87.75°)	1.955 (178.35°)	2.101 (86.56°)	2.005 (169.67°)	1.929 (84.72°)	1.980 (173.69°)	1.909 (82.41°)	2.063 (175.55°)	1.768 (75.37°)
		2.035		2.164		1.968		2.082		2.027		1.992

https://doi.org/10.1021/acsaenm.5c00313
ACS Appl. Eng. Mater. 2025, 3, 2141−2152

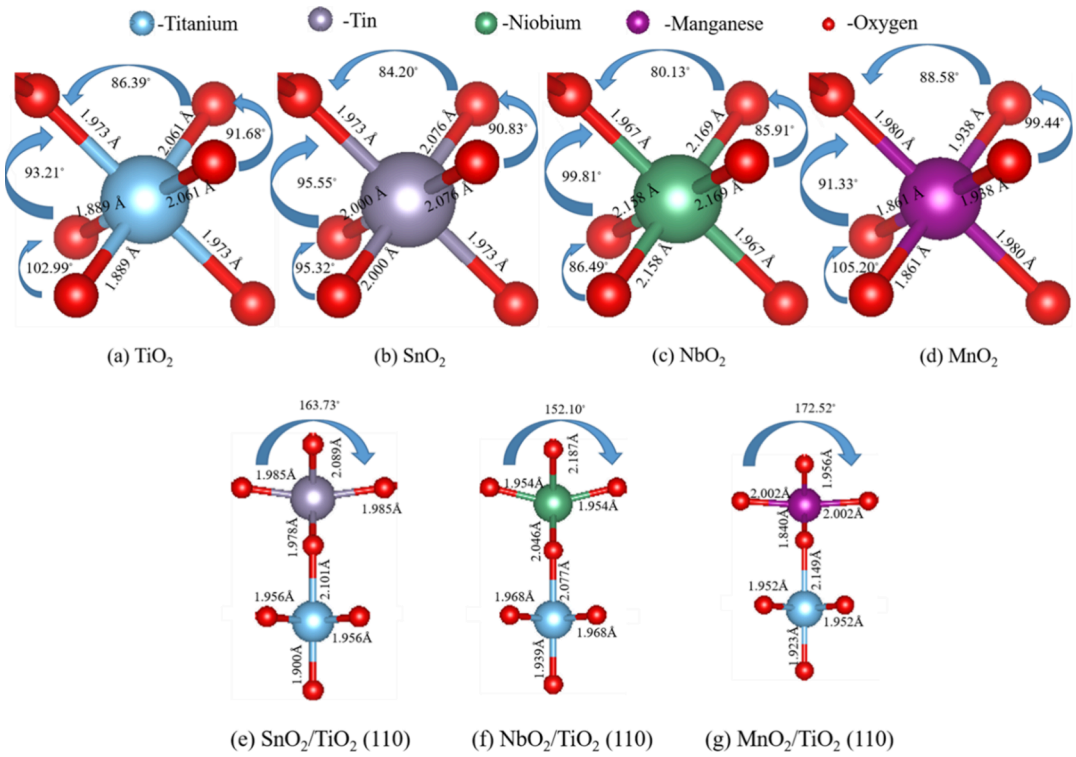

Figure 2. Octahedral distortions of pure (a) TiO_2, (b) SnO_2, (c) NbO_2, (d) MnO_2 rutile (110) surfaces and (e) SnO_2/TiO_2, (f) NbO_2/TiO_2, and (g) MnO_2/TiO_2 heterostructures.

Table 2. Calculated Interfacial Formation Energy of the Rutile(110) Heterostructure and Its Corresponding Calculated Band Gap, Work Function, Bader Charges, Lattice Mismatch, and Oxygen Vacancy Formation Energy

surface	$E_{\text{Form-eng}}$ (eV)	band gap (eV)	work function (eV)	Bader charges	lattice mismatch (%)	O_{2c} vacancy formation energy (eV)
TiO_2		3.26	7.091	Ti = +1.92*e*, O = −0.95*e*		+3.89
SnO_2/TiO_2	−5.1007	1.92	7.262	Sn = +2.32*e*, O = −1.11*e*	7.55	+2.43
NbO_2/TiO_2	−13.0346	0	5.014	Nb = +2.26*e*, O = −1.11*e*	3.64	+4.00
MnO_2/TiO_2	−4.2717	0.56	6.022	Mn = +1.61*e*, O = −0.82*e*	5.59	+2.33

to the monostructure, in the heterostructure model, Nb−O has the longest axial bonds, and Mn−O has the shortest axial bonds.

The lattice mismatch of the heterostructure is shown in Table 2. SnO_2/TiO_2, NbO_2/TiO_2, and MnO_2/TiO_2 heterostructures have lattice mismatches of about 7.55, 3.64, and 5.59%, respectively. Among these, the NbO_2/TiO_2 heterostructure has the minimum lattice mismatch; these results agree well with the previous study on the pseudomorphic heterostructure.[17]

3.2. Interfacial Formation Energy and Oxygen Vacancy

The calculated formation energies are shown in Table 2. All three heterostructures contain the negative formation energy due to the creation of charged layers that occur along the interface of the heterostructure. The negative formation energy is a sign of their thermodynamic stability, indicating the possibility of experimental fabrication of the pseudomorphic (110) heterostructure on top of the TiO_2 rutile(110) surfaces. In the all-heterostructure model, the top layer of the surface strongly binds to the bottom TiO_2 surface. The results are in good agreement with the previous study on the rutile(110) heterostructure.[17] Among the three heterostructures, NbO_2/TiO_2 shows the highest negative formation energy of −13.03 eV, which shows the highest stability among all three heterostructures. The highest interfacial formation energy of the NbO_2/TiO_2 heterostructure is directly attributed to its lowest lattice mismatch (3.64%); hence, it can be considered the most stable among the others. Also, the lowest work function of NbO_2/TiO_2 helps with the ejection of electrons from the surface (Table 2).

In order to reflect the actual physical and chemical environment, the oxygen vacancies are studied at the heterostructures. Among the various oxygen sites, O_{2c} is considered the most common oxygen vacancy.[17] The following formula (eqn 2) was used to study the oxygen vacancy formation energy.

$$E_{\text{Form-eng(Ov)}} = E_{\text{Ov}}^{\text{total}} - E_{\text{pure}}^{\text{total}} + \frac{1}{2}E_{\text{O2}}^{\text{total}} \tag{2}$$

The formation energy of the O_{2c} vacancy on the rutile(110) heterostructure can be studied by calculating the vacancy formation energy of the three heterostructures. equation 2 can be used to calculate the vacancy-interfacial formation energy ($E_{\text{Form-eng}}$(Ov)) of the heterostructure,[17] where $E_{\text{Ov}}^{\text{total}}$ is the total energy of the heterostructure with O_{2c} vacancy, such as SnO_2/TiO_2, NbO_2/TiO_2, and MnO_2/TiO_2; $E_{\text{pure}}^{\text{total}}$ is the total energy of the heterostructure without O_{2c} vacancy, such as SnO_2/TiO_2, NbO_2/TiO_2, and MnO_2/TiO_2; and $E_{\text{O2}}^{\text{total}}$ is known as the total energy of the isolated oxygen molecules. The calculated

https://doi.org/10.1021/acsaenm.5c00313
ACS Appl. Eng. Mater. 2025, 3, 2141−2152

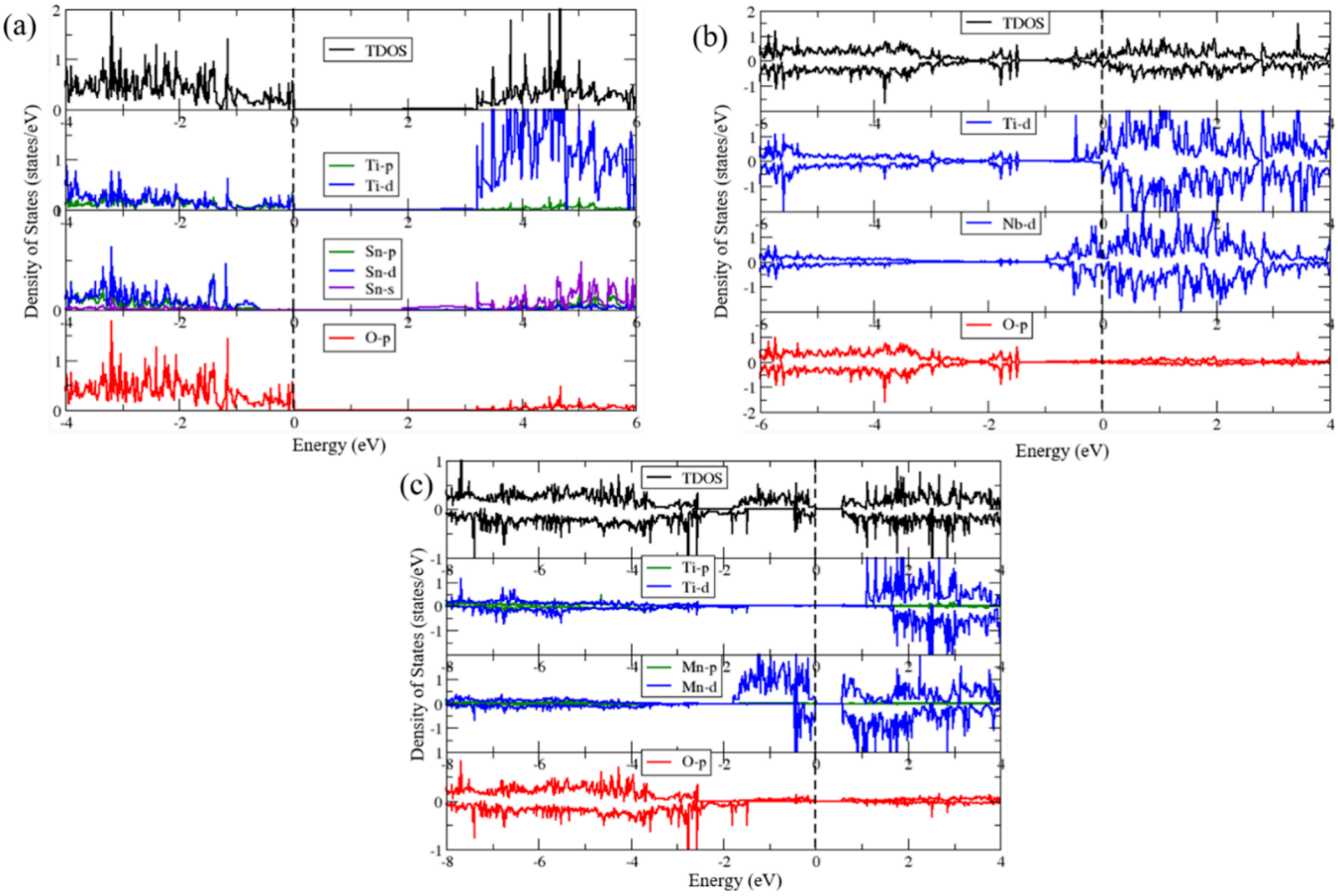

Figure 3. Total density of states (TDOS) and the projected density of states for the SnO_2/TiO_2 (a), NbO_2/TiO_2 (b), and MnO_2/TiO_2 (c) heterostructure.

oxygen vacancy formation energy for the TiO_2 surfaces and the heterostructures is mentioned in Table 2. Among these, the MnO_2/TiO_2 heterostructure has the lowest oxygen vacancy formation energy of about +2.33 eV. The NbO_2/TiO_2 heterostructure has the highest formation energy of about +4.00 eV. Here, the positive oxygen vacancy formation energy represents the required energy for the creation of surface oxygen vacancies. The optimized structure of the heterostructure with an oxygen vacancy is shown in Figure S5 of the Supporting Information.

3.3. Electronic Structure Analysis

The projected density of states (PDOS) by HSE06 calculations for the SnO_2/TiO_2 (a), NbO_2/TiO_2 (b), and MnO_2/TiO_2 (c) heterostructure is shown in Figure 3, and that for the monostructure of (110) surfaces of TiO_2, SnO_2, NbO_2, and MnO_2 is shown in Figure S1 of the Supporting Information. From the hybrid functional calculation (HSE06), we obtained the band gap values of 3.26 and 4.43 eV, respectively, for the $TiO_2(110)$ and $SnO_2(110)$ surfaces. The previously calculated band gap values of $TiO_2(110)$ and $SnO_2(110)$ surfaces were 3.1[34] and 3.6 eV,[35] respectively. Due to the mixing parameter in the hybrid functional calculations, we get slightly overestimated band gap values for SnO_2.[36] In the electronic structure of the TiO_2 (110) surface (Figure S1a in the Supporting Information), the valence band is predominantly formed by O-2p orbitals, and the conduction band is predominantly formed by Ti-3d orbitals. For the $SnO_2(110)$ surface (Figure S1b), the valence band is mainly dominated by O-2p orbitals, whereas the conduction band is mainly dominated by Sn-5s orbitals. The PDOS of the $SnO_2/TiO_2(110)$ heterostructure is shown in Figure 3a, and we obtained the calculated band gap value of the SnO_2/TiO_2 heterostructure, which is 1.92 eV. The valence band maximum (VBM) of the heterostructure is mainly dominated by the hybridized orbitals of O-2p and Ti-3d, respectively. In the inner valence band, from −0.5 eV onward, it has the hybridization of Ti-3d, Sn-4d, and O-2p orbitals. The conduction band minimum (CBM) is mainly dominated by Sn-5s orbitals, whereas the inner conduction band from 2.5 eV onward is predominantly formed by Ti-3d orbitals. From the electronic structure analysis, it is found that the SnO_2/TiO_2 heterostructure has a type II heterostructure, which can be explained by further analysis. Our results agree well with the previously studied SnO_2/TiO_2 heterostructure.[18]

The PDOS for the $NbO_2/TiO_2(110)$ heterostructure is shown in Figure 3b. From the literature, it is known that rutile NbO_2 of the $P4_2/mnm$ space group shows a metallic nature.[37,35] The calculated PDOS for the $NbO_2(110)$ monostructure is shown in Figure S1c in the Supporting Information, where the Fermi level falls on the Nb-4d states. The valence band is dominated by the O-2p orbitals, whereas the conduction band is dominated by the Nb-4d orbitals. Our electronic structure plots agree well with the previous study on rutile NbO_2.[38] The PDOS of the $NbO_2/TiO_2(110)$ heterostructure, as shown in Figure 3b, also shows the metallic nature, where the Nb-4d states cross the Fermi level. Apart from Nb-4d, Ti-3d also crosses the Fermi level, thus indicating

https://doi.org/10.1021/acsaenm.5c00313
ACS Appl. Eng. Mater. 2025, 3, 2141−2152

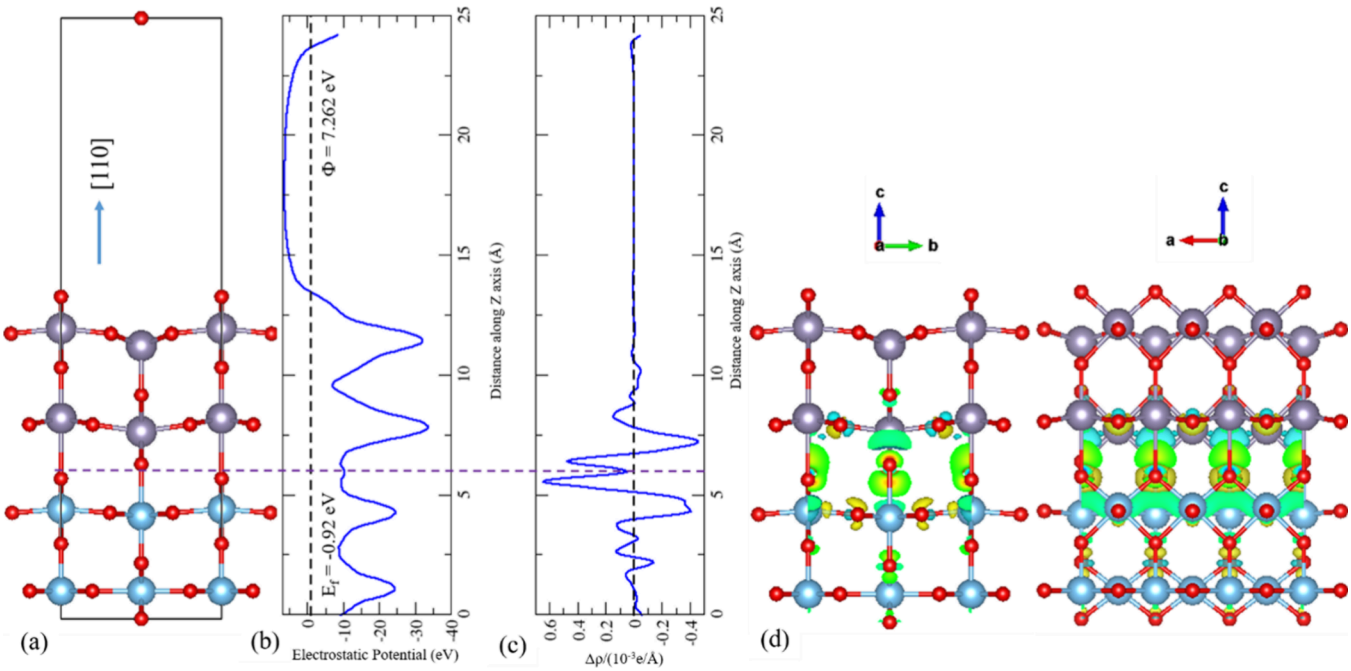

Figure 4. Calculated electrostatic potential and charge density difference analysis of the SnO_2/TiO_2 heterostructure. Heterostructure model with *Z*-direction (a), electrostatic potential plot (b), planar average charge density plot (c), and charge density difference plots (d).

the flow of charges from NbO_2 to TiO_2. The inner valence band is predominantly formed by the O-2p orbitals. The conduction band minimum is formed by the hybridization of Ti-3d and Nb-4d orbitals. From our PDOS plots of the $NbO_2/TiO_2(110)$ heterostructure, it was found that there were significant differences in the band alignment between the Ti-3d and Nb-4d bands, which leads to creating the internal electric field along the interface, thus enhancing the separation of electron and hole charge carriers. Unlike the SnO_2/TiO_2 heterostructure (semiconductor−semiconductor interface), the NbO_2/TiO_2 heterostructure shows the metal−semiconductor interface.[17] The crystal field splitting of the e_g and t_{2g} orbitals of Nb-4d states was analyzed by the orbital projected density of states, as shown in Figure S2 in the Supporting Information.

The PDOS for the $MnO_2/TiO_2(110)$ heterostructure is shown in Figure 3c. The PDOS for the $MnO_2(110)$ monostructure is shown in Figure S1d of the Supporting Information. The calculated band gap of the $MnO_2(110)$ surface is 0.43 eV, which agrees well with the previously calculated band gap.[39] The conduction band and the valence band maximum are predominantly formed by Mn-3d orbitals, and the inner valence bands (from −2.0 eV onward) are only formed by the O-2p orbitals. For the case of the $MnO_2/TiO_2(110)$ heterostructure, the calculated band gap value is about 0.56 eV. In the PDOS of the MnO_2/TiO_2 heterostructure (Figure 3c), the conduction band minimum is only formed by Mn-3d orbitals, whereas the inner conduction band from 1 eV onward is predominantly dominated by a hybridized form of both Ti-3d and Mn-3d orbitals. The valence band maximum is formed only by the Mn-3d orbitals, and the inner valence band from 2.0 eV is mainly dominated by the O-2p orbitals. From the electronic structure analysis, it is concluded that in the $MnO_2/TiO_2(110)$ heterostructure, both the VBM and CBM are formed by only Mn-3d orbitals, unlike SnO_2/TiO_2 and NbO_2/TiO_2 heterostructures. Hence, it is concluded that it shows a type I heterostructure, which can be explained by further analysis. From the antiferromagnetic calculation, the calculated magnetic moment for Mn is about 2.66 μ_B. Figures S3 and S4 show the PDOS for the $MnO_2(110)$ surface and MnO_2/TiO_2 heterostructure, respectively.

3.4. Electrostatic Potential, Charge Density Difference, and Bader Charge Analysis

The creation of an internal electric field and the nature of the charge flow mechanism between the interface of the heterostructure are further studied by electrostatic potential, charge density difference, and Bader charge analysis. The calculated electrostatic potential along the *Z*-axis for the SnO_2/TiO_2 heterostructure is shown in Figure 4b. The calculated work function for the SnO_2/TiO_2 heterostructure is about 7.262 eV, which is known as the amount of energy required to remove an electron from the Fermi level to vacuum.[40] From 0 to 6 Å, the potential goes up to −25 eV, which corresponds to the TiO_2 layers. From 6 to 13 Å, the potential increases to −35 eV, corresponding to the SnO_2 layers. However, the overall potential along the *Z*-axis is the same due to the symmetric layers of the SnO_2/TiO_2 heterostructure. The planar average charge density difference plot for the SnO_2/TiO_2 heterostructure is shown in Figure 4c, which can be calculated by subtracting the monostructure charge density of SnO_2 and TiO_2 from the SnO_2/TiO_2 heterostructure charge density. In the planar average charge density difference plot, the positive values describe the charge accumulation region, and the negative values describe the charge depletion region. The interface of the heterostructure is mentioned by the violet dotted lines in Figure 4. From the plot, it was found that there is a strong creation of an internal electric field along the interface of the heterostructure. There was the transfer of an electron from the SnO_2 layer to the TiO_2 layer, which can be understood by the highest negative peak at 7−8 Å on the SnO_2 side and the highest positive peak at 5−6 Å on the TiO_2 side. The highest negative and positive peaks are going up to −0.4

https://doi.org/10.1021/acsaenm.5c00313
ACS Appl. Eng. Mater. 2025, 3, 2141−2152

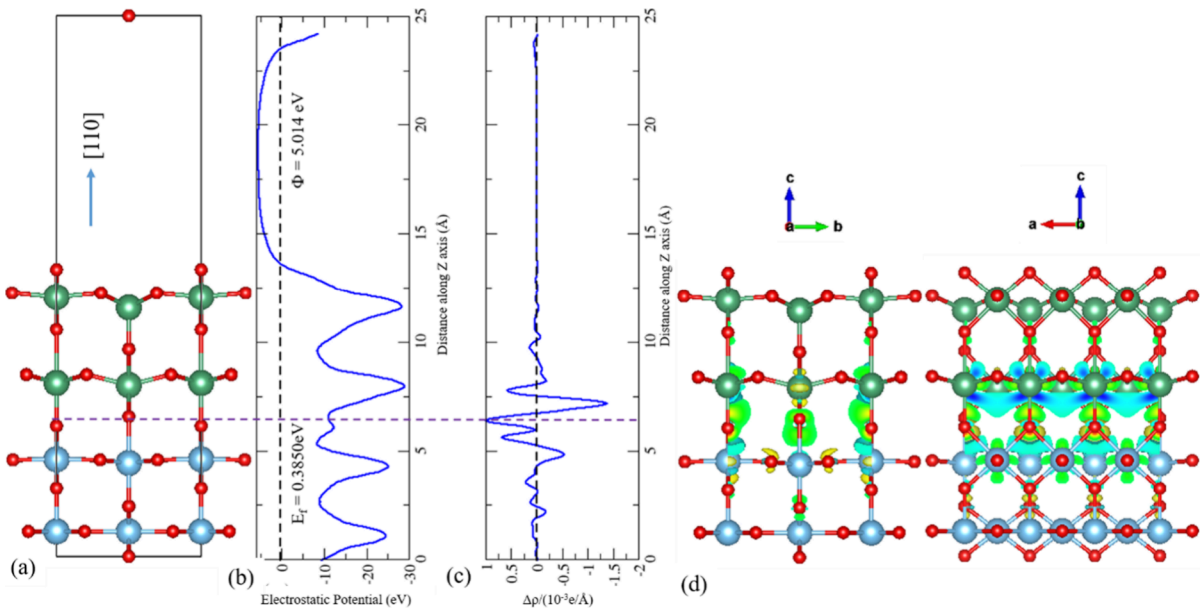

Figure 5. Calculated electrostatic potential and charge density difference analysis of the NbO_2/TiO_2 heterostructure. Heterostructure model with *Z*-direction (a), electrostatic potential plot (b), planar average charge density plot (c), and charge density difference plots (d).

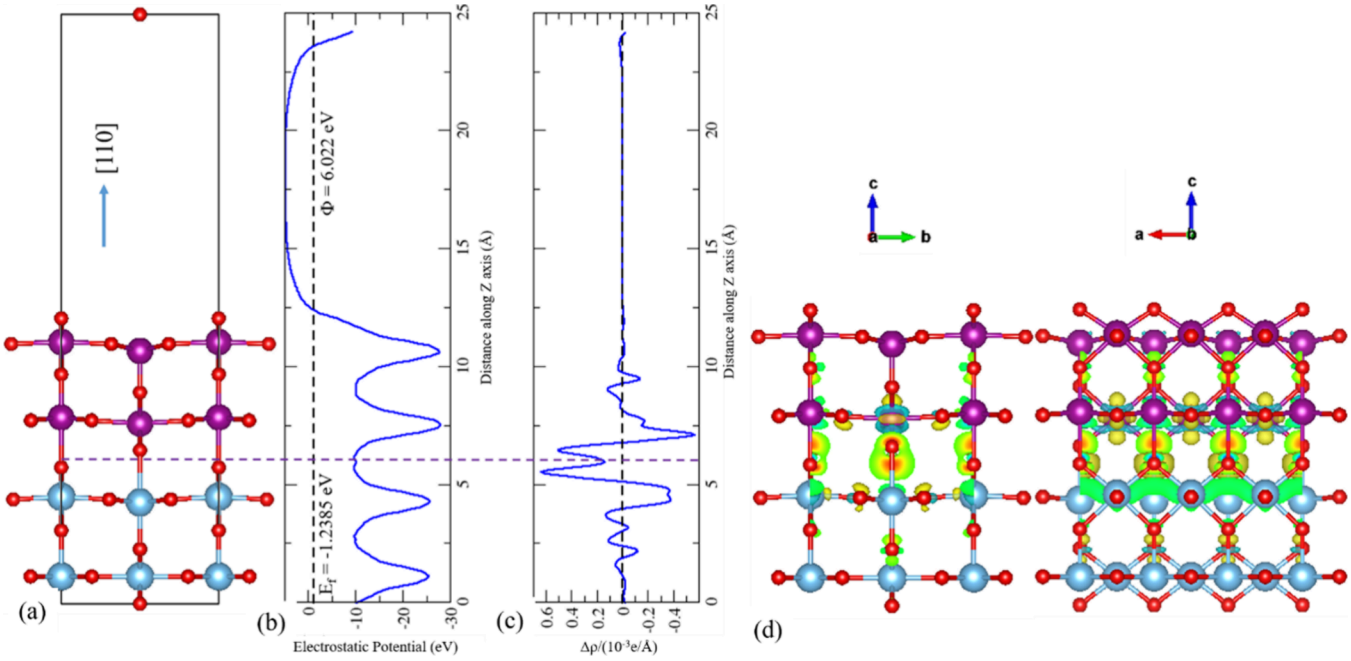

Figure 6. Calculated electrostatic potential and charge density difference analysis of the MnO_2/TiO_2 heterostructure. Heterostructure model with *Z*-direction (a), electrostatic potential plot (b), planar average charge density plot (c), and charge density difference plots (d).

and 0.6 $\Delta\rho$, respectively. The Bader charge analysis shows an increase in charge after constructing the heterostructure for Sn and O atoms, with values of +2.32*e* and −1.11*e*, respectively, which is higher than the pure TiO_2 (please see Table 2). This can be further confirmed by charge density difference plots shown in Figure 4d, where the charge accumulation is denoted by a yellow color, and the charge depletion is denoted by a cyan color. There was a depletion of charges at the SnO_2 layer and an accumulation of charges at the TiO_2 layer. These results confirm that there was the creation of an internal electric field and the flow of electrons from SnO_2 to TiO_2 layers. Our results agree well with the previous work.[18] The transfer of charge carriers from SnO_2 to TiO_2 through the interface proves that it came under the category of a type II heterostructure. The band alignment for this type II heterostructure is explained in the next section. The creation of an internal electric field leads to enhanced separation of electron and hole charge carriers, which will eventually increase the photocatalytic application of the heterostructure compared to the pristine material.[41]

The calculated electrostatic potential along the *Z*-axis for the NbO_2/TiO_2 heterostructure is shown in Figure 5b. The work function for this heterostructure is 5.014 eV, which is very low compared to other structures and improves the extraction of electrons. The electrostatic potential value for the TiO_2 layers, from 0 to 6 Å, goes up to −25 eV, while for the NbO_2 layers, from 6 to 13 Å, it goes up to −28 eV. There was a small

https://doi.org/10.1021/acsaenm.5c00313
ACS Appl. Eng. Mater. 2025, 3, 2141−2152

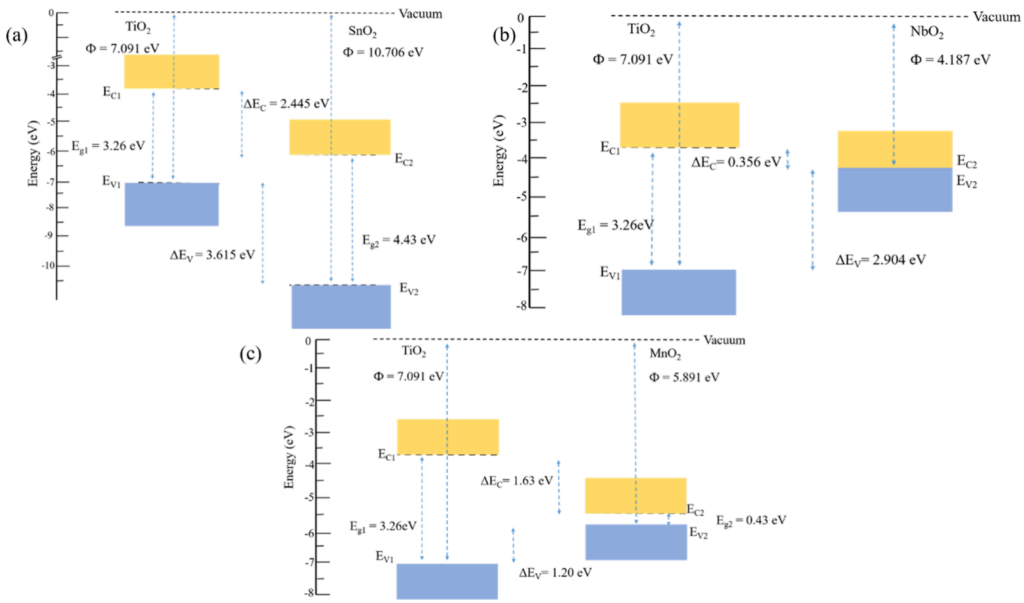

Figure 7. Calculated band edge position for the SnO_2/TiO_2 (type II) (a), NbO_2/TiO_2 (metal−semiconductor interface) (b), and MnO_2/TiO_2 (type I) (c) heterostructure to vacuum potential.

fluctuation in the electrostatic potential along the interface at 6 Å of the heterostructure. The creation of the internal electric field along the interface of the heterostructure can be explained by the charge density difference plot. The calculated planar average charge density difference plot for the NbO_2/TiO_2 heterostructure is shown in Figure 5c. From the plot, it is observed that the highest negative peaks appeared at 7−8 Å in the NbO_2 layer, whereas the highest positive peak appeared at 6 Å in the TiO_2 layer of the heterostructure. The highest negative and positive peaks go up to −1.5 and 1.0 $\Delta\rho$, respectively. The Bader charge analysis shows an increase in charge after constructing the heterostructure for Nb and O atoms, with values of +2.26e and −1.11e, respectively, which is higher than the pure TiO_2 (please see Table 2). Hence, there was a flow of electrons from the NbO_2 layers into the TiO_2 layers due to the strong creation of an internal electric field. Our results agree well with the previously studied experimental Nb_2O_5/TiO_2 heterostructure.[42] These can be further explained by the charge density difference plots shown in Figure 5d, where the charge depletion occurs at NbO_2 layers and the charge accumulation occurs at TiO_2 layers of the heterostructure. There will be higher possibilities of the separation of electron and hole charge carriers compared to the pristine TiO_2. The quantity of charge flow between the NbO_2/TiO_2 heterostructure is higher than the SnO_2/TiO_2 heterostructure.

The calculated electrostatic work function for the MnO_2/TiO_2 heterostructure is shown in Figure 6b. The work function value of the heterostructure is about 6.022 eV. The electrostatic potential for TiO_2 layers, from 0 to 6 Å, goes up to −25 eV, while for MnO_2 layers, from 6 to 13 Å, it goes up to −28 eV. Due to the symmetric layers of the heterostructure between TiO_2 and MnO_2, there were no considerable fluctuations in the electrostatic potential. The calculated planar average charge density difference plot for the MnO_2/TiO_2 heterostructure is shown in Figure 6c. The highest negative peak appeared in 7−8 Å in the MnO_2 layer, whereas the highest positive peak appeared in 5−6 Å in the TiO_2 layer of the heterostructure. The highest negative and the positive peaks go up to −0.5 and 0.6 $\Delta\rho$, respectively. The Bader charge analysis shows a decrease in charge after constructing the heterostructure for Mn and O atoms, with values of +1.61e and −0.82e, respectively, which is lower than the pure TiO_2 (please see Table 2). Hence, there was a flow of electrons from the TiO_2 layer to the MnO_2 layers by the creation of an internal electric field. The creation of charge depletion on MnO_2 layers and the charge accumulation on TiO_2 layers can be visualized by the charge density difference plot, as shown in Figure 6d.

3.5. Band Alignment

The schematic representation of the calculated band offsets for the vacuum potential is shown in Figure 7. For the $SnO_2/TiO_2(110)$ heterostructure, the band alignment is shown in Figure 7a because the calculated work function is 7.091 and 10.706 eV for TiO_2 and SnO_2, respectively. The work function value is considered as the difference between the VBM and the vacuum level. Here, the vacuum level is set to zero. The calculated band gap values for TiO_2 and SnO_2 are 3.26 and 4.43 eV, respectively. Hence, for TiO_2, the CBM lies at 3.831 eV, and for SnO_2, it lies at 6.276 eV. The SnO_2/TiO_2 heterostructure has a difference in valence band energy (ΔE_V) and conduction band energy (ΔE_C), which are 3.615 and 2.455 eV, respectively. From the band alignment, we conclude that, after the irradiation of sunlight, electrons get excited from the VBM into the CBM, and the hole remains in the VBM. Furthermore, there will be a flow of electron charge carriers from the CBM of TiO_2 to the CBM of SnO_2 and also a flow of hole charge carriers from the VBM of SnO_2 to the VBM of TiO_2. Hence, there was an accumulation of electrons on the CBM of TiO_2 and an accumulation of holes on the VBM of SnO_2. The flow of electron and hole charge carriers leads to the creation of an internal electric field on the interface of the heterostructure. Our band offset calculations agreed well with the previously reported theoretical and experimental evidence of the type II heterostructure of SnO_2/TiO_2.[18,43]

The calculated band alignment for the NbO_2/TiO_2 heterostructure is shown in Figure 7b. The calculated work function of NbO_2 is 4.187 eV. Both the CBM and VBM of

https://doi.org/10.1021/acsaenm.5c00313
ACS Appl. Eng. Mater. 2025, 3, 2141−2152

NbO_2 lie at 4.187 eV. The NbO_2/TiO_2 heterostructure has ΔE_V and ΔE_C values of 2.904 and 0.356 eV, respectively. From the band alignment calculation, we concluded that, in the NbO_2/TiO_2 heterostructure, there were possibilities of the flow of electron charge carriers from the CBM of TiO_2 to the CBM of NbO_2 and the flow of hole charge carriers from the VBM of TiO_2 to the VBM of NbO_2.

The calculated band alignment for the MnO_2/TiO_2 heterostructure is shown in Figure 7c. The calculated work function and band gap of MnO_2 are calculated to be 5.891 and 0.43 eV, respectively. The CBM and VBM values of MnO_2 lie at 5.461 and 5.891 eV, respectively. The MnO_2/TiO_2 heterostructure has ΔE_V and ΔE_C values of 1.20 and 1.63 eV, respectively. From the band offset calculation, it is concluded that there was a flow of electron charge carriers from the CBM of TiO_2 to the CBM of MnO_2 and a flow of hole charge carriers from the VBM of TiO_2 to the VBM of MnO_2. Hence, it is concluded that the MnO_2/TiO_2 heterostructure shows the type I heterostructure, and our prediction on band alignment agrees well with the previously reported experimental work.[20]

3.6. Chemical Bonding Analysis

To understand the chemical bonding between the heterostructure, the charge density analysis and ELF are plotted. The top row in Figure 8a−c represents the charge density plots, and

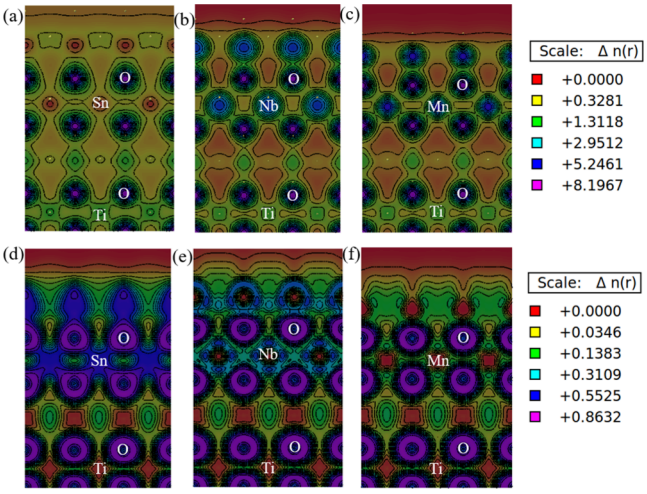

Figure 8. Charge density analysis along the (010) plane for SnO_2/TiO_2 (a), NbO_2/TiO_2 (b), and MnO_2/TiO_2 (c) heterostructure. ELF along the (010) plane for SnO_2/TiO_2 (d), NbO_2/TiO_2 (e), and MnO_2/TiO_2 (f) heterostructure.

the bottom row in Figure 8d−f represents the ELF plots. In all the figures, the MO_2 layers (SnO_2, NbO_2, and MnO_2), are seen at the top of the TiO_2 layers. Most of the charge density is only accumulated around the O atom of the heterostructure. Both charge density and ELF plots show the ionic bonding characteristics of Ti−O bonds. From our previous analysis, Ti−O bonds are considered iono-covalent, i.e., ionic bonds with non-negligible covalent characters.[44,4] From charge density and ELF plots, it is found that there was clear ionic bonding for SnO_2 layers. There was no sharing of electrons between the Sn and O atoms (Figure 8a,d). The charge density plots and ELF plots for the NbO_2/TiO_2 heterostructure are shown in Figure 8b,e, respectively. From both charge density and ELF plots, NbO_2 shows the ionic bonding characteristics; however, there were some non-negligible covalent characteristics. There was the sharing of electrons on axial bonds between Nb and O of the top layer of the heterostructure. Hence, the axial Nb−O bonds exhibit a more covalent nature than the planar Nb−O bonds. The charge density and ELF plots for the MnO_2/TiO_2 heterostructure are shown in Figure 8c,f, respectively. From both charge density and ELF plots, it is found that the Mn−O bonds of the MnO_2 layers show an ionic bonding nature. The charge accumulation occurs at both the Mn and O atoms. However, there was some non-negligible covalent interaction between the Mn−O bonds in its axial bonds. There was a non-negligible sharing of electrons between the O^{2+} and Mn^{4+} atoms.

3.7. Optical Absorption

The calculated optical absorption spectra for the $SnO_2/TiO_2(110)$, $NbO_2/TiO_2(110)$, and $MnO_2/TiO_2(110)$ heterostructures and $TiO_2(110)$ plots are shown in Figure 9, as a

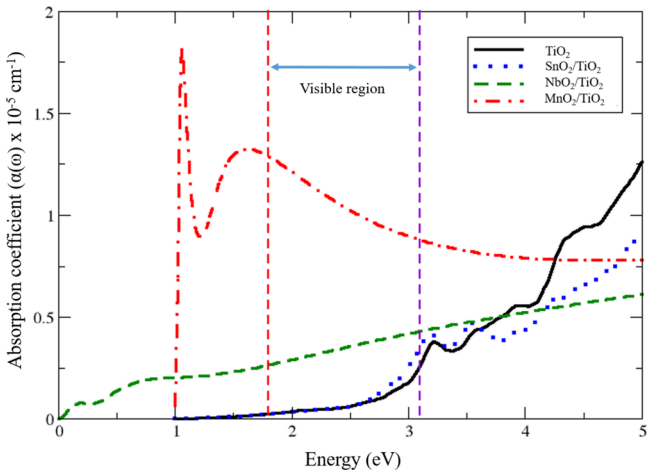

Figure 9. Optical absorption spectrum plots for the SnO_2/TiO_2, NbO_2/TiO_2, and MnO_2/TiO_2 heterostructures and the TiO_2 layer.

function of energy (eV). The visible region in the solar spectrum from 1.8 to 3.1 eV is mentioned in the absorption plot. Since the optical excited state calculation was carried out in the GGA calculation, the scissor operation is carried out to overcome the band gap difference between the GGA and HSE calculations. From the absorption plot, the following conclusions are understood. The SnO_2/TiO_2 heterostructure shows poor optical absorption compared to pure TiO_2, and it is active only in the UV region of the solar spectrum. Both the NbO_2/TiO_2 and MnO_2/TiO_2 heterostructures show a long range of optical absorption in the IR, visible, and UV regions. Due to the higher number of electron charge carriers, the NbO_2/TiO_2 and MnO_2/TiO_2 heterostructures show improved optical absorption in both the IR and visible region spectra. Compared with NbO_2/TiO_2, the MnO_2/TiO_2 heterostructure has a higher optical absorption coefficient. Hence, these can be used as potential photocatalysts for environmental pollution reduction.[46] Optical absorption by the conventional GGA functionals underestimates the band gap. Here, the scissor operation has been included to overcome the optical band gap underestimation by the GGA functional.

3.8. Improvement in Photocatalytic Activity

The structural part discusses the geometrical microstructure upon modeling the different transition metal oxides on TiO_2

https://doi.org/10.1021/acsaenm.5c00313
ACS Appl. Eng. Mater. 2025, 3, 2141−2152

surfaces along the (110) direction. The variation in bond length, bond angle, and the octahedral distortion at the surface and the interface of the heterostructure is clearly studied. The variation in structural modification at the three variants of the heterostructure is thoroughly studied. The thermodynamic stability of the heterostructure interface and the possibility of oxygen vacancy formation are analyzed by interfacial formation and the oxygen vacancy formation energetics. The variation in stability along the three heterostructures is analyzed. The band gap tuning is achieved by heterostructure formation, with the aid of the HSE06 functional. The reduction in the band gap helps us to achieve visible-light-active photocatalytic activity. Now, the ultraviolet-active photocatalyst is turned into a visible-light-active photocatalyst. Now, the material is able to harvest 40% of the solar spectrum. Earlier, it was hardly restricted to using only 5% of the solar spectrum. The generation of electron and hole charge carriers plays an important role in the photocatalytic activity of the materials, which is further involved in the photocatalytic redox reaction and other mechanisms. Unfortunately, pure TiO_2 has a short lifetime of electron and hole charge carriers and the highest probability of the recombination of those charge carriers. The drawback can be overcome by the formation of the heterostructure model. The creation of an internal electric field and interfacial charge transfer process is further confirmed by the charge density difference and Bader charge analysis. The internal electric field created on the interface of the heterostructure can reduce the possibility of recombination of electron charge carriers. If the recombination of charge carriers is reduced, it can be able to perform enhanced photocatalytic reactions with the aid of electron and hole charge carriers. Furthermore, the work function and band alignment analysis are carried out in order to further explore the photocatalytic mechanism of the heterostructure. The nature of the type of heterostructure is explored. The optical absorption studies further validate the improvement in the possibilities of photocatalytic activity, as compared to pure TiO_2, NbO_2/TiO_2, and MnO_2/TiO_2 heterostructures, which exhibit improved optical absorption in both the ultraviolet and visible regions of the solar spectrum.

4. CONCLUSIONS

The pseudomorphic rutile(110) heterostructure of SnO_2/TiO_2, NbO_2/TiO_2, and MnO_2/TiO_2 was modeled and studied by the DFT formalism. The bond length and angle between the different layers of the heterostructure were analyzed. The variation in the octahedral distortion was understood. From the interfacial formation energy calculation, all the heterostructures have negative formation energy. Among these, NbO_2/TiO_2 has the highest negative formation energy and the lowest lattice mismatch; hence, it will be thermodynamically more stable. From the hybrid functional calculation (HSE06), the electronic structure and the band gap for the SnO_2/TiO_2, NbO_2/TiO_2, and MnO_2/TiO_2 heterostructures were studied. The conduction and valence band energy states and their orbital hybridizations were analyzed by the density of states plots of the heterostructure. The creation of an internal electric field on the interface of the heterostructure is considered an important phenomenon, which further causes the enhanced separation of electron and hole charge carriers and eventually increases the photocatalytic activity of the material. The creation of an internal electric field on the rutile heterostructure is confirmed, and the accumulation and depletion of charges are further studied by the charge density difference plot; the possibility of the transport of electron and hole charge carriers is understood. The nature of the type of heterostructure is analyzed by the band alignment calculation. From our prediction, it is understood that SnO_2/TiO_2 shows type II heterostructure characteristics, MnO_2/TiO_2 shows type I heterostructure characteristics, and NbO_2/TiO_2 shows the metal−semiconductor interface. The relative electron and hole charge carriers' transport mechanism was further understood by the band alignment calculation. The improvement in the optical absorption toward the visible spectrum of the heterostructure is confirmed by the optical absorption coefficient plot. Compared to the pristine TiO_2, both NbO_2/TiO_2 and MnO_2/TiO_2 heterostructures show good optical absorption in both the IR and visible spectra. The internal electric field of the pseudomorphic rutile(110) heterostructure was explored, the nature of the type of heterostructure was found, and its band alignment was calculated. A possible way to tune the heterostructure toward enhanced photocatalytic activity is proposed. From our theoretical calculations, we strongly concluded that the growth of the rutile heterostructure on top of TiO_2 will act as a potential photocatalyst for environmental pollution reduction and also for other photocatalytic applications. We believe that our results will attract researchers from both the experimental and theoretical communities for further studies.

■ ASSOCIATED CONTENT

Supporting Information

The Supporting Information is available free of charge at https://pubs.acs.org/doi/10.1021/acsaenm.5c00313.

Band structure plots, projected density of states plots, table of lattice parameters, and images of the optimized structure with O-vacancy (PDF)

■ AUTHOR INFORMATION

Corresponding Author

R. Vidya − *Centre for Materials Informatics (C-MaIn), Sir. C.V. Raman Science Block and Computational Laboratory for Multifunctional Materials (CoLaMM), Department of Physics, Anna University, Chennai 600025, India;* orcid.org/0000-0002-7798-1797; Email: vidyar@annauniv.edu

Authors

S. Muthukrishnan − *Centre for Materials Informatics (C-MaIn), Sir. C.V. Raman Science Block and Computational Laboratory for Multifunctional Materials (CoLaMM), Department of Physics, Anna University, Chennai 600025, India*

Anja Olafsen Sjåstad − *Centre for Materials Science and Nanotechnology, Department of Chemistry, University of Oslo, Oslo N-0315, Norway;* orcid.org/0000-0001-9280-541X

Complete contact information is available at: https://pubs.acs.org/10.1021/acsaenm.5c00313

Author Contributions

S.M.: conceptualization, investigation, data curation, formal analysis, analysis, collection, and writing—original draft. R.V.: conceptualization, investigation, data curation, formal analysis,

analysis, collection, and writing—original draft. A.O.S.: investigation and formal analysis.

Notes

The authors declare no competing financial interest.

■ ACKNOWLEDGMENTS

The authors are grateful to the University of Oslo, Norway, for providing the financial grant through the Indo-Norway project titled "Oxide Surfaces for Nitrous Oxide Abatement" (CIR/60/INDO-NORWAY/2019). The authors are also thankful to the SCANMAT Centre, Central University of Tamil Nadu, India, for computing time.

■ REFERENCES

(1) Ali, I.; Suhail, M.; Alothman, Z. A.; Alwarthan, A. Recent advances in syntheses, properties and applications of TiO_2 nanostructures. *RSC Adv.* **2018**, *8* (53), 30125−30147.

(2) Fujishima, A.; Honda, K. Electrochemical Photolysis of Water at a Semiconductor Electrode. *Nature* **1972**, *238*, 37−38.

(3) Etacheri, V.; Di Valentin, C.; Schneider, J.; Bahnemann, D.; Pillai, S. C. Visible-light activation of TiO_2 photocatalysts: Advances in theory and experiments. *J. Photochem. Photobiol., C: Photochem. Rev.* **2015**, *25*, 1−29.

(4) Muthukrishnan, S.; Vidya, R.; Sjåstad, A. O. Band gap engineering of anatase TiO_2 by ambipolar doping: A first-principles study. *Mater. Chem. Phys.* **2023**, *299*, No. 127467.

(5) Lun Pang, C.; Lindsay, R.; Thornton, G. Chemical reactions on rutile TiO_2(110). *Chem. Soc. Rev.* **2008**, *37* (10), 2328−2353.

(6) Huyen, T. T. T.; Chi, T. T. K.; Dung, N. D.; Kosslick, H.; Liem, N. Q. Enhanced Photocatalytic Activity of {110}-Faceted TiO_2 Rutile Nanorods in the Photodegradation of Hazardous Pharmaceuticals. *Nanomaterials* **2018**, *8*, 276.

(7) Low, J.; Yu, J.; Jaroniec, M.; Wageh, S.; Al-Ghamdi, A. A. Heterojunction Photocatalysts. *Adv. Mater.* **2017**, *29* (20), No. 1601694.

(8) Lin, Y.; Ren, P.; Wei, C. Fabrication of MoS_2/TiO_2 heterostructures with enhanced photocatalytic activity. *CrystEngComm* **2019**, *21* (22), 3439−3450.

(9) Sood, S.; Mehta, S. K.; Sinha, A. S. K.; Kansal, S. K. Bi_2O_3/TiO_2 heterostructures: Synthesis, characterization and their application in solar light mediated photocatalyzed degradation of an antibiotic, ofloxacin. *Chem. Eng. J.* **2016**, *290*, 45−52.

(10) Yao, L.; Li, X.; Liu, H.; Li, Z.; Lu, Q. One-dimensional hierarchical $CeVO_4/TiO_2$ heterostructures with enhanced photocatalytic performance. *J. Nanopart. Res.* **2019**, *21*, 140.

(11) Li, Y.; Wang, L.; Liang, J.; Gao, F.; Yin, K.; Dai, P. Hierarchical Heterostructure of ZnO@TiO_2 Hollow Spheres for Highly Efficient Photocatalytic Hydrogen Evolution. *Nanoscale Res. Lett.* **2017**, *12*, 531.

(12) Rajput, R. B.; Jamble, S. N.; Kale, R. B. A review on TiO_2/SnO_2 heterostructures as a photocatalyst for the degradation of dyes and organic pollutants. *J. Environ. Manage.* **2022**, *307*, No. 114533.

(13) Aguirre, M. E.; Zhou, R.; Eugene, A. J.; Guzman, M. I.; Grela, M. A. Cu2O/TiO2 heterostructures for CO2 reduction through a direct Z-scheme: Protecting Cu_2O from photocorrosion. *Appl. Catal., B* **2017**, *217*, 485−493.

(14) Trenczek-Zajac, A.; Banas-Gac, J.; Radecka, M. TiO_2@Cu_2O n-n Type Heterostructures for Photochemistry. *Materials* **2021**, *14*, 3725.

(15) Mannaa, M. A.; Qasim, K. F.; Alshorifi, F. T.; El-Bahy, S. M.; Salama, R. S. Role of NiO Nanoparticles in Enhancing Structure Properties of TiO_2 and Its Applications in Photodegradation and Hydrogen Evolution. *ACS Omega* **2021**, *6* (45), 30386−30400.

(16) Wang, Q.; Zhang, W.; Hu, X.; Xu, L.; Chen, G.; Li, X. Hollow spherical WO_3/TiO_2 heterojunction for enhancing photocatalytic performance in visible-light. *J. Water Process Eng.* **2020**, *40*, No. 101943.

(17) Wei, W.; Dai, Y.; Huang, B.; Li, X.; Nägele, F.; Over, H.; Whangbo, M.-H.; Jacob, T. Density Functional Characterization of the Electronic Structures and Band Bending of Rutile RuO_2/TiO_2(110) Heterostructures. *J. Phys. Chem. C* **2015**, *119* (22), 12394−12399.

(18) Zhou, Y. d.; Liu, Q. L.; Yang, C.; Zhao, Z. Y. Interfacial microstructure and properties of TiO_2/SnO_2 heterostructures with rutile phase: A DFT calculation investigation. *Appl. Surf. Sci.* **2018**, *451*, 258−271.

(19) Wang, H.; Liu, J.; Xiao, X.; Meng, H.; Wu, J.; Guo, C.; Zheng, M.; Wang, X.; Guo, S.; Jiang, B. Engineering of SnO_2/TiO_2 heterojunction compact interface with efficient charge transfer pathway for photocatalytic hydrogen evolution. *Chin. Chem. Lett.* **2023**, *34*, 107125.

(20) Zhang, Y.; Wu, M.; Kwok, Y. H.; Wang, Y.; Zhao, W.; Zhao, X.; Huang, H.; Leung, D. Y. C. In-situ synthesis of heterojunction TiO_2/MnO_2 nanostructure with excellent performance in vacuum ultraviolet photocatalytic oxidation of toluene. *Appl. Catal., B* **2019**, *259*, No. 118034.

(21) Ma, Q.; Wang, H.; Zhang, H.; Cheng, X.; Xie, C.; Cheng, Q. Fabrication of MnO_2/TiO_2 nano-tube arrays photoelectrode and its enhanced visible light photoelectrocatalytic performance and mechanism. *Sep. Purif. Technol.* **2017**, *189*, 193−203.

(22) Kresse, G.; Furthmüller, J. Efficiency of ab-initio total energy calculations for metals and semiconductors using a plane-wave basis set. *Comput. Mater. Sci.* **1996**, *6*, 15−50.

(23) Kresse, G.; Furthmüller, J. Efficient iterative schemes for ab initio total-energy calculations using a plane-wave basis set. *Phys. Rev. B* **1996**, *54*, 11169−11186.

(24) Perdew, J. P.; Burke, K.; Ernzerhof, M. Generalized gradient approximation made simple. *Phys. Rev. Lett.* **1996**, *77*, 3865−3868.

(25) Kresse, G.; Joubert, D. From ultrasoft pseudopotentials to the projector augmented-wave method. *Phys. Rev. B* **1999**, *59*, 1758−1775.

(26) Hu, K.; Wu, M.; Hinokuma, S.; Ohto, T.; Wakisaka, M.; Fujita, J. i.; Ito, Y. Boosting electrochemical water splitting: via ternary NiMoCo hybrid nanowire arrays. *J. Mater. Chem. A* **2019**, *7*, 2156−2164.

(27) Heyd, J.; Scuseria, G. E.; Ernzerhof, M. Hybrid functionals based on a screened Coulomb potential. *J. Chem. Phys.* **2003**, *118*, 8207−8215.

(28) Momma, K.; Izumi, F. VESTA 3 for three-dimensional visualization of crystal, volumetric and morphology data. *J. Appl. Crystallogr.* **2011**, *44*, 1272−1276.

(29) Wang, V.; Xu, N.; Liu, J. C.; Tang, G.; Geng, W. T. VASPKIT: A user-friendly interface facilitating high-throughput computing and analysis using VASP code. *Comput. Phys. Commun.* **2021**, *267*, No. 108033.

(30) Kokalj, A. XCrySDen-a new program for displaying crystalline structures and electron densities. *J. Mol. Graph. Model.* **1999**, *17*, 176−179.

(31) Yang, Z.; Wu, R.; Zhang, Q.; Goodman, D. W. First-principles study of the adsorption of CO on TiO2(110). *Phys. Rev. B* **2001**, *63*, No. 045419.

(32) Labat, F.; Baranek, P.; Domain, C.; Minot, C.; Adamo, C. Density functional theory analysis of the structural and electronic properties of TiO_2 rutile and anatase polytypes: performances of different exchange-correlation functionals. *J. Chem. Phys.* **2007**, *126*, 154703.

(33) Sanches, F. F.; Mallia, G.; Harrison, N. M. Simulating constant current STM images of the rutile TiO_2 (110) surface for applications in solar water splitting. *Mater. Res. Soc. Symp. Proc.* **2013**, *1494*, 339−344.

(34) Yu, Y.; Yang, X.; Zhao, Y.; Zhang, X.; An, L.; Huang, M.; Chen, G.; Zhang, R. Engineering the Band Gap States of the Rutile TiO_2 (110) Surface by Modulating the Active Heteroatom. *Angew. Chem., Int. Ed.* **2018**, *57*, 8550.

https://doi.org/10.1021/acsaenm.5c00313
ACS Appl. Eng. Mater. 2025, 3, 2141−2152

(35) Maki-Jaskari, M. A.; Rantala, T. T. Band structure and optical parameters of the SnO2 (110) surfaces. *Phys. Rev. B* **2001**, *64*, No. 075407.
(36) Park, S.; Lee, B.; Jeon, S. H.; Han, S. Hybrid functional study on structural and electronic properties of oxides. *Curr. Appl. Phys.* **2011**, *11*, S337−S340.
(37) Eyert, V. The metal-insulator transition of NbO_2: An embedded Peierls instability. *Europhys. Lett.* **2002**, *58*, 851−856.
(38) O'Hara, A.; Nunley, T. N.; Posadas, A. B.; Zollner, S.; Demkov, A. A. Electronic and optical properties of NbO_2. *J. Appl. Phys.* **2014**, *116*, 213703.
(39) Kitchaev, D. A.; Peng, H.; Liu, Y.; Sun, J.; Perdew, J. P.; Ceder, G. Energetics of MnO_2 polymorphs in density functional theory. *Phys. Rev. B* **2016**, *93*, No. 045132.
(40) Kruthika, G.; Ravindran, P. Understanding the optoelectronic properties of interface between Cs_2TiBr_6 and TiO_2 for solar cell applications. *Mater. Today Commun.* **2022**, *32*, No. 103963.
(41) Ashwin Kishore, M. R.; Larsson, K.; Ravindran, P. Two-dimensional Cd_X/C_2N (X = S, Se) heterostructures as potential photocatalysts for water splitting: A DFT study. *ACS Omega* **2020**, *5*, 23762−23768.
(42) Yan, J.; Wu, G.; Guan, N.; Li, L. Nb_2O_5/TiO_2 heterojunctions: Synthesis strategy and photocatalytic activity. *Appl. Catal., B: Environ.* **2014**, *152−153*, 280−288.
(43) Deb, M.; Ghossoub, Y.; Noel, L.; Li, P. H.; Tsai, H. Y.; Soppera, O.; Zan, H. W. Highly Efficient UV-Activated TiO2/SnO2 Surface Nano-matrix Gas Sensor: Enhancing Stability for ppb-Level NOx Detection at Room Temperature. *ACS Appl. Mater. Interfaces* **2025**, *17*, 14670−14681.
(44) Sousa, C.; Illas, F. Ionic-covalent transition in titanium oxides. *Phys. Rev. B* **1994**, *50*, 13974.
(45) Zhang, S.; Dai, M.; Guo, J.; Wang, G.; Wang, S.; He, Z. Stable Ti^{3+} in B-TiO_2/BN based hybrids for efficient photocatalytic reduction. *Chem. Eng. J. Adv.* **2022**, *11*, No. 100333.
(46) Wang, G.; Zhou, T.; Wang, S. Editorial: Semiconductor Photocatalysts. *Crystals* **2023**, *13*, 1109.
(47) Tang, W.; Sanville, E.; Henkelman, G. A grid-based Bader analysis algorithm without lattice bias. *J. Phys.: Condens. Matter* **2009**, *21*, No. 084204.
(48) Junquera, J.; Cohen, M. H.; Rabe, K. M. Nanoscale smoothing and the analysis of interfacial charge and dipolar densities. *J. Phys.: Condens. Matter* **2007**, *19*, No. 213203.
(49) Silvi, B.; Savin, A. Classification of chemical bonds based on topological analysis of electron localization functions. *Nature* **1994**, *371*, 683−686.
(50) Muthukrishnan, S.; Vidya, R.; Sjåstad, A. O. Illustrating the surface chemistry of nitrogen oxides (NOx) adsorbed on rutile TiO_2 (110) with the aid of STM and AIMD simulation. *Catal. Sci. Technol.* **2025**, *15*, 1850−1864.

https://doi.org/10.1021/acsaenm.5c00313
ACS Appl. Eng. Mater. 2025, 3, 2141−2152